Dynamics of point defect formation, clustering and pit initiation on the pyrite surface

F.W. Herbert [a,c,d,1], A. Krishnamoorthy [a,c,1], W. Ma [b,c], K.J. Van Vliet [a,d], B. Yildiz [b,c,*]

[a] *Department of Materials Science and Engineering, Massachusetts Institute of Technology, Cambridge, Massachusetts 02139, USA*
[b] *Department of Nuclear Science and Engineering, Massachusetts Institute of Technology, Cambridge, Massachusetts 02139, USA*
[c] *Laboratory for Electrochemical Interfaces, Massachusetts Institute of Technology, Cambridge, Massachusetts 02139, USA*
[d] *Laboratory for Material Chemomechanics, Massachusetts Institute of Technology, Cambridge, Massachusetts 02139, USA*

ABSTRACT

The collective behavior of point defects formed on the free surfaces of ionic crystals under redox conditions can lead to initiation of local breakdown by pitting. Here, we controllably generated sulfur vacancies on single crystal $FeS_2(100)$ through *in vacuo* annealing, and investigated the resulting evolution of surface chemistry using synchrotron x-ray photoelectron spectroscopy (XPS). By measuring the S $2p$ photoemission signal intensity arising from sulfur defects as a function of temperature, the enthalpy of formation of sulfur vacancies was found to be 0.1 ± 0.03 eV, significantly lower than the reduction enthalpy of bulk FeS_2. Above 200 °C, the created sulfur vacancies together with preexisting iron vacancies condensed into nm-scale defect clusters, or pits, at the surface, as evidenced by scanning tunneling microscopy (STM). We provide a mechanistic description for the initiation of pits that requires the concerted behavior of both the sulfur and iron vacancies, and validate this model with kinetic Monte Carlo (kMC) simulations. The model probes realistic length and time scales, providing good agreement with the experimental results from XPS and STM measurements. Our results mechanistically and quantitatively describe the atomic scale processes occurring at pyrite surfaces under chemically reducing environments, important in many natural and technological settings, ranging from its role as a passivating film in corrosion to its potential use as a photovoltaic absorber in solar energy conversion.

© 2014 Elsevier Ltd. All rights reserved.

1. Introduction

Iron disulfide (FeS_2), or pyrite, is a stable Fe-S phase that has received considerable attention in a range of technological and geochemical processes. It is established that FeS_2 can form in sulfidic corrosion scales on iron alloy-based oilfield structures, where dissolved H_2S and oxidizers such as low-valent sulfur (polysulfide, sulfite, thiosulfate) are present [1]. In these anoxic environments at working temperatures up to 200 °C, surface interactions with molecular species such as H_2S, H_2O, H_2, and CH_3 (and their derivatives S^{2-}, HS^-, etc.) are important in the formation, growth and stability of pyrite as a passivating film component on steel [2]. Furthermore, the oxidation of pyrite by H_2O and O_2 is responsible for ground water acidification (i.e., "acid mine drainage"),[3] and FeS_2-H_2S interactions have been proposed as an energy source

for primitive life [4]. Technologically, pyrite has been used as a cathode in Li-ion batteries [5–7] and its application as an earth-abundant photovoltaic (PV) absorber has also received renewed interest due to its promising optical properties [8]. Experimental reports of relatively low open circuit voltages (<200 mV) in pyrite devices–as compared with an optical band gap energy E_g of $\approx$ 0.95 eV [9–13]–have recently motivated a re-examination of the bulk [14] and surface [15] electronic properties of FeS_2.

Given this range of contexts motivated by pyrite defect composition and chemistry, this paper aims to elucidate two interconnected phenomena in which surface vacancies on pyrite play an important role. First is the chemical degradation of corrosion-passivating films, typically ionic compounds formed by reactions between metallic surfaces and molecular species in the environment. Anion and cation vacancy condensation is a key process postulated by the Point Defect Model (PDM) for the growth and breakdown of passive films on metallic surfaces in contact with aqueous corrosive solutions [16,17]. Both on metals and on ionic passive films, clustering of point defects (vacancies) is thought to be necessary for pit initiation, the rate-controlling step in overall pitting corrosion

[18]. This process has been observed on pure metals [19–21] and alloys [22–24]. On the other hand, understanding the surface pitting mechanism on ionic passive films has been a challenge, experimentally limited to only few successfully studied systems such as Ni-O, Ni-OH and Cr_2O_3, [25–27] and without a concerted modeling and experimental demonstration at the atomic scale. Even in simpler systems such as pure metals and semiconductors, where surface pitting is relatively better understood, modeling of surface degradation is generally limited to the use of empirical kinetic parameters. Matching simulated time scales to experimental ones has remained challenging and has lacked experimental validation of model results [28–32]. Here we take pyrite as a model passive film system for investigating the surface pitting process at the atomic spatial scale and the experimental time scales. Vacancy formation and pitting are not induced electrochemically in this work, but rather via *in situ* annealing of FeS_2(100) single crystals at different temperatures up to 330 °C under ultra-high vacuum (UHV) conditions. Recalling that our FeS_2(100) single crystals were synthesized under sulfur-rich conditions, the experimental conditions which are sulfur-poor in UHV here form a strong driving force to create sulfur vacancies and pull iron vacancies from the bulk to the surface. We are careful to contrast this with typical aqueous corrosion environments, under which the primary driving force for cation vacancy formation is an applied electric field which induces cation dissolution at the material surface. In this work we rely on the large chemical potential gradient *in vacuo*, coupled with thermal activation to provide the energy for point defect formation and migration- more akin to 'dry corrosion' or 'scaling' that occurs at elevated temperatures in the absence of water. Despite this difference, the formation of cation and anion vacancies observed in pitting conditions could be induced either chemically or electrochemically as long as the effective chemical potentials are equivalent. Thus our approach permits a highly resolved observation of incipient pitting in ionic materials under carefully controlled and clean conditions.

The second aspect of this investigation, which is complementary to the first, regards the unresolved non-stoichiometry of pyrite surfaces, which cannot be explained based on defect chemistry of the bulk material. Native point defect concentrations in bulk FeS_2 are generally low ($O(10^6)$ cm^{-3}) at room temperature [33,34] and this is important for the performance of pyrite as a passivating thin film in corrosion as well as a PV absorber. On the other hand, anionic vacancies, specifically sulfur vacancies denoted as V_S, are expected to be far more prevalent at free surfaces, with calculated formation enthalpies as low as 0.4 eV [35,36]. This has led to difficulties in obtaining surfaces with low intrinsic defect concentrations in nanocrystalline pyrite precursors and films [10,13,37–41]. Sulfur deficiency is typically put forward as a source of non-ideal electronic and optical properties in synthetic FeS_2. However, there remains a need to experimentally quantify the formation energy of V_S on the surface to understand whether these defects are indeed a significant source of off-stoichiometry in pyrite surfaces.

The crystal structure of pyrite is NaCl-type cubic, with Fe^{2+} at the cation site and S_2^{2-} dimers at the anion site, aligned along the cube diagonal <111>. The (100) surface of FeS_2 is unreconstructed and is the most stable surface, as shown by low energy electron diffraction (LEED) [42,43] and scanning tunneling microscopy (STM) [44,45]. The sulfur S 2*p* x-ray photoemission peak of pyrite, when accessed using soft x-ray synchrotron radiation, reveals highly detailed information about the different binding environments of sulfur in the near-surface region. In addition to the dimer S_2^{2-} signal from the crystal bulk, pyrite's S 2*p* photoelectron spectrum distinguishes two additional, surface-localized and coordinately reduced sulfur environments at more negative binding energies [46–49]. Quantification of these surface-localized defect environments enables further understanding of the two open areas summarized above.
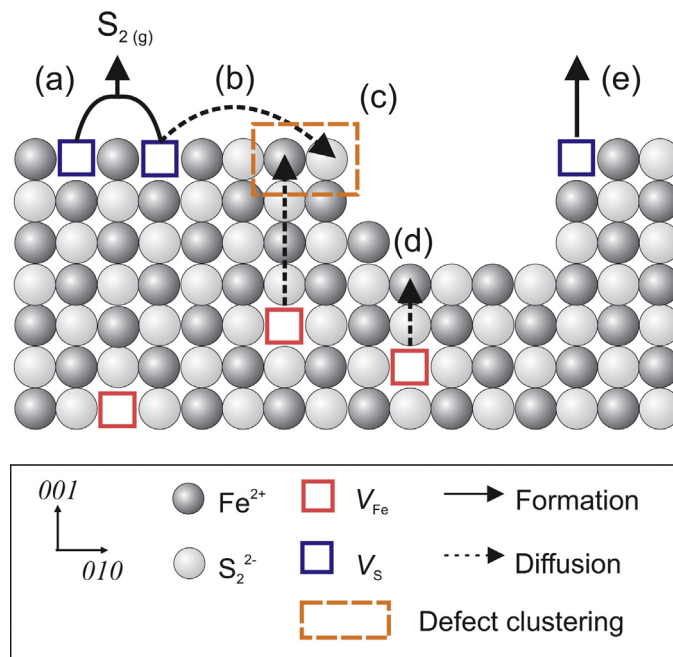
Fig. 1. Illustration of atomic processes involved in the proposed mechanism of pit formation and growth on pyrite (100). (a) Formation of surface sulfur monovacancies V_S through evaporation into vacuum. (b) Diffusion of V_S to a pit site. (c) Agglomeration of vacancies on the iron and sulfur sublattices by diffusion, leading to the initiation and growth of the pit. Presence of an initiated pit (as depicted in this figure) is not a necessary precursor to the process in (c). (d) Iron vacancies, denoted as V_{Fe}, that are already present in the bulk migrate to the surface during annealing. (e) V_S formation at under-coordinated sites surrounding pits has lower formation enthalpy as compared to isolated vacancy formation process in (a).

The concentration of defects at each stage was evaluated using the S 2*p* peak from synchrotron XPS and quantified by systematic peak fitting, allowing us to estimate the enthalpy of sulfur vacancy formation. In addition, we demonstrated using STM that upon reduction in UHV at temperatures in excess of 200 °C, surface defects aggregate to form clusters of up to 10 nm in width and exactly one-half or one lattice parameter in depth. We identified three basic atomistic processes–vacancy formation, vacancy annihilation and vacancy diffusion–which, in tandem, lead to the formation of the observed pits. The mechanism combining these unit processes, described in Fig. 1, was validated using a kinetic Monte Carlo (kMC) model of the FeS_2 (100) surface.

Our experiments and computational model demonstrate how point defects in both cation and anion sublattices in ionic solids can condense at elevated temperatures to form nanoscale surface pits. The defect formation and diffusion processes required for such a phenomenon are key assumptions in the point defect models for describing the passive film breakdown in extreme redox environments [50,51]. The low formation enthalpy for V_S supports the hypothesis that FeS_2 surfaces are off-stoichiometric and highly reducible, with detrimental implications for the performance of pyrite-containing passive films and synthetic pyrite-based devices.

2. Methods

2.1. Experimental Methods

Single crystal pyrite samples were synthesized by chemical vapour transport (CVT) in the presence of Br as a transport agent, as described in Ref. [15]. Growth faces were identified to be primarily (100) by electron back-scattered diffraction (EBSD; Zeiss Supra-55 scanning electron microscope). Phase purity of both

the poly- and single-crystalline synthesized pyrite was confirmed using Raman spectroscopy and X-ray diffraction. We note that the synthesis of FeS_2 single crystals was performed under a high partial pressure of sulfur. Although the pyrite phase has a stoichiometric ratio of Fe/S = 0.5 in the bulk in ambient conditions, such sulfur-rich growth conditions are expected to favor the incorporation of iron vacancies in the bulk, consistent with previous calculations of defect formation energies as a function of sulphur chemical potential [34,52]. After cooling of the as-synthesized crystals at ∼ 5 °C/min under sulfur-rich conditions inside quartz tubes, a non-equilibrium high concentration of V_{Fe} remained quenched within the bulk FeS_2. We propose these quenched-in iron vacancies to be a source of iron vacancies near/on the surface under the reducing environment (i.e., under a low chemical potential of sulfur) during our subsequent experiments. This is because elevated temperatures assist in migration of iron vacancies to the surface from the bulk that has become supersaturated in iron vacancies, as the bulk evolves toward thermal equilibrium with a lower vacancy concentration. The role of such iron vacancies on the surface is discussed in more detail in Section 3.

Synchrotron x-ray photoelectron spectroscopy (XPS) was performed at Brookhaven National Lab (Upton, NY) at the U12A beam line of the National Synchrotron Light Source, in order to deduce the temperature dependence and the formation enthalpy of surface defects. The radiation source was tuneable, monochromatized soft x-rays in the energy range 100-600 eV with a resolution ΔE/E of 2×10^{-2}–10^{-3} and spot size of 1 mm^2 on the sample surface. The base pressure in the vacuum chamber remained below 10^{-10} Torr for the duration of the experiment. Clean single crystal FeS_2 samples with (100)-oriented growth faces larger than 5×5 mm^2 were prepared by ultrasonication in acetone then methanol in an inert atmosphere glove box, before being mounted in a mechanical sample clamp. During transfer into the UHV environment, the samples were limited to <5 min air exposure to minimize surface oxidation and other contamination. We did not observe any secondary peaks from sulfates or other oxidation products [53]. Controllable, *in situ* heating between 120-330 °C at steps of 30 °C was achieved using a resistively-heated coil placed behind the sample. The heating apparatus and sample stage were cooled collectively by flowing liquid N_2 through the manipulator, which was attached to the sample via a large copper block. Each *in situ* annealing cycle lasted 150 min, which was adequate for the pyrite surface to reach equilibrium with the UHV base pressure; subsequently, the sample was allowed to cool to ∼100 K for XPS measurements in order to quench in the surface chemistry and also minimize phonon broadening of the XPS signal. S 2p photoemission spectra were obtained at excitation energies of 210, 350 and 500 eV with an energy resolution of 100 meV and pass energy of 10 eV. Peak fitting of the S 2p XPS spectra was carried out using CasaXPS Version 2.3.16. Shirley background subtraction was applied to all spectra and individual components were fit with 95% Gaussian-5% Lorentzian peak distributions, unless otherwise specified.

Scanning tunneling microscopy (STM) images were collected in order to visualize the evolution of surface defects at elevated temperatures. An STM system (Omicron VT-STM; Omicron Nanotechnology, GmbH, Germany) was used under UHV conditions below 10^{-9} Torr. Electrochemically etched PtIr tips were annealed in the chamber at 150 °C to clean them prior to taking measurements. FeS_2 samples used for STM/STS were synthesized and prepared in a manner similar to that described above for the XPS experiments. STM images were subjected to a global flattening procedure and horizontal noise removal using SPIP 4.8.4 software from Image Metrology (Denmark).

2.2. Density Functional Theory (DFT) calculations

Density Functional Theory (DFT) calculations were conducted to quantify energy barriers for the formation, diffusion and agglomeration of surface point defects at the atomic level. All DFT calculations [54] were carried out with projector augmented wave method [55] using the Vienna Ab-initio Simulation Package (VASP) [56,57] using the Perdew-Burke-Ernzerhof (PBE) form of the GGA functional [58] with spin polarization included. Activation barriers for the surface diffusion process were calculated using the Climbing Image Nudged Elastic Band (CINEB) method [59] with five images on $2 \times 2 \times 2$ unit cell slabs of the pyrite (100) surface separated by 10 Å of vacuum. The thickness of the slab and the vacuum condition were chosen such that the surface energy of the (100) surface converged to within 0.03 J/m^2. In all slab calculations, the topmost two surface layers of S-Fe-S were allowed to relax while the other layers remained fixed at positions consistent with bulk pyrite. The reciprocal space was sampled with a $4 \times 4 \times 1$ Monkhorst-Pack grid [60] and integrated over with a Gaussian smearing (σ=0.1 eV). DFT + U corrections were applied using the previously calculated value of U-J = 1.6 eV [52]. All calculations were performed with a plane wave cut-off energy of 350 eV. Total energies for each image were converged to within 10^{-5} eV in each self-consistency cycle. The forces on ions were converged to within 0.01 eV/Å for each image. All crystal structures shown were generated using the VESTA visualization program [61].

2.3. Kinetic Monte Carlo simulations

Kinetic Monte Carlo (kMC) simulations [62] were performed on a model of the pyrite (100) surface to understand the processes responsible for the experimentally observed defect structure and concentrations. The kMC method permits us to describe the time-evolution of the system structure under non-equilibrium conditions or towards an equilibrium state. Towards this end, we attempt to identify a kMC model made up of a small set of elementary processes that can reproduce the experimentally observed phenomena. In particular, our aim is to elucidate the mechanisms of both surface pit initiation and the non-Arrhenius variation of the vacancy concentration at elevated temperatures.

The simulated model system consisted of a FeS_2 slab containing $110 \times 110 \times 2$ lattice sites under periodic boundary conditions in the lateral direction. This corresponds to a real-life sample of lateral size 30 nm × 30 nm and a height of 1 unit cell, appropriate for modeling surface processes. Each lattice site was initially occupied by either a Fe^{2+} of S_2^{2-} ion organized in a checkerboard pattern to reproduce the NaCl-type crystal structure. In this model, Fe^{2+} sites can exist in one of two states (vacant or occupied by a Fe^{2+} ion) and S_2^{2-} sites can exist in one of three possible states (occupied by a S_2^{2-} dimer ion, occupied by a single S^{2-} ion indicating the presence of a monomer vacancy, V_S, or fully vacant with a dimer vacancy).

The effective time for system evolution depends on the activation energy barriers of the elementary processes included in the kMC model. Here, we modeled two elementary processes occurring in tandem: surface vacancy formation and surface vacancy diffusion. The probability of occurrence of each process, j, at a temperature T is given by the Arrhenius equation, $j = \nu \exp\left(-E_b/k_B T\right)$, where ν is the attempt frequency, E_b the activation barrier, and k_B the Boltzmann's constant. For surface vacancy diffusion, only the jumps between nearest neighbors of the same species were considered. For example, V_{Fe} was allowed to move only to the nearest-neighbor site containing a Fe^{2+} ion, and V_S only to a nearest-neighbor site containing a monomer vacancy or S_2^{2-} ion. Vacancy formation processes were allowed to occur on any site that is not already completely vacant. To satisfy detailed balance requirements, each vacancy formation process

also included a corresponding vacancy annihilation process, which was allowed to occur on any site that is not completely occupied (i.e., it was allowed on Fe^{2+} vacancies, S^{2-} monomer vacancies and S_2^{2-} dimer vacancies). The barriers for the different elementary processes described in our kMC model were obtained in part by our DFT calculations, in part from our experiments, and in part by fitting to reproduce experimental observations. Activation energy barriers for the surface diffusion process were obtained from DFT and CINEB, as this process is well-defined at the atomic level, down to atomic trajectories. Activation barriers for Fe and S vacancy formation and annihilation processes were obtained via empirical fitting to reproduce experimental time-scales and experimentally observed vacancy concentrations; these barriers are rather intractable using *ab initio* calculations, due to both a multiplicity of pathways that must be sampled and the contributions of gaseous species' entropic contributions that are not captured via DFT. Finally, difference between the activation barriers of vacancy formation and annihilation were constrained by the formation enthalpy determined by our XPS experiments. It is important to note that the strength of the kMC models rests not on the exact values used for the activation energy barriers but on its ability to explain emergence of complex phenomena mechanistically as an interaction among a small number of elementary unit processes.

Since all the elementary processes described so far involve the formation or breaking of bonds around a lattice site, we make the reasonable assumption that the activation energy barriers for the processes depend upon the coordination number of the site under consideration. More specifically, we implement a bond-counting model where the activation barrier for each elementary process depended linearly on the number of bonds broken during the process, an approach that has been applied in previous kMC studies [31,63]. In our model, local site coordination was sampled using the parameter N_{bb} given by

$$N_{bb} = \frac{\text{Number of neighboring defect free sites}}{4}$$

Here, the denominator of 4 is equal to the theoretical maximum number of defects around a lattice site in our checkerboard model. Using this parameter, vacancy formation processes were modeled to have an energy barrier, $E_{t,vf}$, of the form

$$E_{t,vf} = E_t^0 + (\alpha \times N_{bb})$$

where E_t^0 is a neighborhood-independent constant barrier for the process, and α is a scaling parameter that represents the dependence of activation barriers on site coordination. According to equation (1), the value of α is the change in the barrier for vacancy formation between a site where $N_{bb} = 1$ (a fully coordinated site) and $N_{bb} = 0$ (a hypothetical, fully uncoordinated site). This is equivalent to the energy required to break all nearest-neighbor bonds, i.e. to create a vacancy in a full-coordinated site. Therefore, the value of α is chosen to be of the same order as the experimentally measured surface vacancy formation enthalpy of 0.10 eV.

Conversely, vacancy annihilation processes (which can be thought of as processes leading to the filling-in of an existing vacancy by formation of bonds with occupied nearest-neighbor sites) are expected to become easier (i.e., have a lower activation energy barrier) with increased site coordination. Therefore, vacancy annihilation processes are modeled to have an energy barrier, $E_{t,va}$ of the form

$$E_{t,va} = E_t^0 - (\alpha \times N_{bb})$$

The activation barriers for the surface vacancy diffusion process have a similar form, given by

$$E_{t,diff} = E_{t,diff}^0 - \left(\alpha \times N_{bb}^t - N_{bb}^f\right)$$

Table 1
Activation energy barriers for elementary unit processes in the kMC model.

Elementary unit process	Activation energy barrier range (eV)
E_t^0 for V_{Fe} formation	1.49 - 1.59
E_t^0 for V_S formation	1.57 - 1.67
E_t^0 for V_{Fe} annihilation	1.49 - 1.59
E_t^0 for V_S annihilation	1.57 - 1.67
E_t^0 for surface diffusion	1.40 - 1.50

Here, N_{bb}^f is the neighborhood sampling parameter at the site from which the vacancy initially diffuses and N_{bb}^t is the neighborhood sampling parameter at the final site to which the vacancy moves. If the selected vacancy diffusion process breaks more bonds than it re-forms, the activation barrier for the process is higher; if the selected vacancy diffusion process breaks fewer bonds than it re-forms, the activation barrier for the process is lower.

Due to the partial empiricism in the identification of the activation barriers, in particular E_t^0 and α, additional kMC calculations were conducted to assess model sensitivity to these parameters. The range of E_t^0 values for each process explored in this study is given in Table 1. In addition, the value of alpha was also sampled from 0.05 eV to 0.1 eV. For the reminder of the paper, we will refer to calculations conducted using activation barriers equal to the mean of the range given in Table 1: $V_{S,form} = 1.62$ eV, $V_{S,anni} = 1.62$ eV, $V_{Fe,form} = 1.54$ eV, $V_{Fe,anni} = 1.64$ eV, $V_{diff} = 1.45$ eV.

3. Results and discussion

We first demonstrate how the surface of FeS_2 evolves under the reducing conditions of the ultra-high vacuum environment and increasingly high temperature, through the initial formation of sulfur monovacancies and the migration to the surface of iron vacancies that were supersaturated in the bulk crystal. At a sufficiently high temperature of ~240 °C, vacant cation and anion sites were observed to coalesce into pits of <100 nm in lateral dimension and of either exactly one-half or one lattice parameter depth. We employed the kMC model to propose an atomistic mechanism for this phenomenon at realistic time and length scales. The results have implications for degradation of ionic passive films in extreme redox environments, and shed light on the facile nature of sulfur vacancy formation at the surface of FeS_2, a long-standing hypothesis for the sulfur deficiency typically measured in synthetic, polycrystalline pyrite.

3.1. Evolution of surface structure and chemistry

We examined the formation of individual and clustered point defects on the (100) surface of pyrite under successive reduction at increasing temperatures in the UHV environment. The approach to gather element-specific signatures around an x-ray absorption site included analysis of core holes that result from core-level ionization and x-ray absorption. Fig. 2 shows a series of four S 2p spectra taken on single crystal FeS_2(100) to illustrate the effects of varying the annealing temperature (210 °C and 330 °C, as labeled), as well as the source excitation energy (350 eV in Fig. 2a and 2b; 210 eV in Fig. 2c and 2d). The experimental data were deconvoluted by peak fitting into three doublet components, consistent with the well-established S 2p features of pyrite [46–48,64,65]. Here, we adopt the nomenclature introduced by Andersson et al. [48] for the features B, S and M, as described below. The spin-orbit splitting 2p3/2 peak was fixed for each component at 1.18 eV above the corresponding 2p1/2 peak, with an intensity ratio of 1:2 for the doublet pairs. Further constraints used in peak fitting are
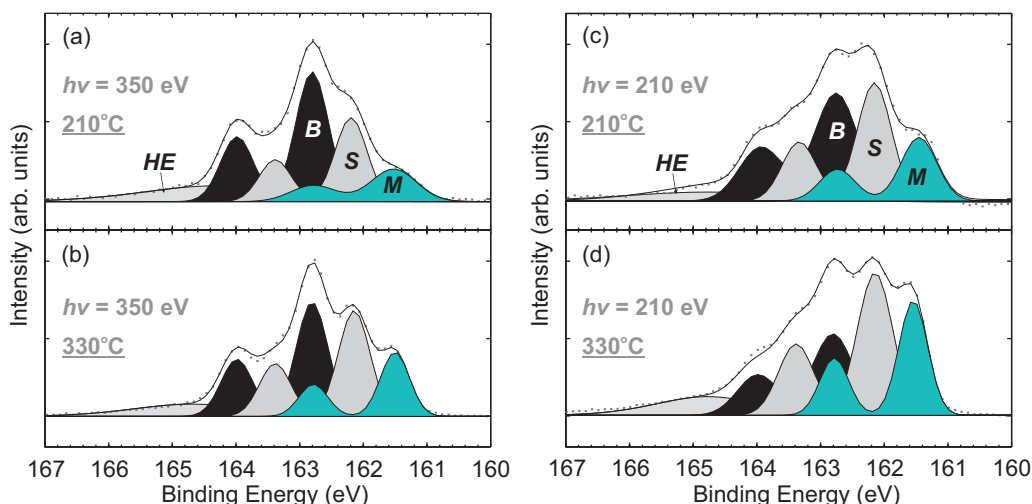
Fig. 2. S 2p photoelectron spectra of FeS$_2$(100) at excitation energies $h\nu$ of (a, b) 350 eV and (c, d) 210 eV after annealing in ultra-high vacuum at 210 °C and 330 °C, respectively. The recorded XPS data points are shown as dots and solid lines mark the enveloping curve from peak fitting. Three features, labeled B, S and M are fit to the experimental data. Components S and M grow in intensity from 210-330 °C and are more prominent when probed with the lower 210 eV excitation energy, consistent with the surface localization of these features.

Table 2
Core level shift (CLS), relative to the bulk pyrite dimer signal B, and full width half maximum (FWHM) of fitted S 2p peaks (B, S, M and HE) used for quantification.

Excitation Energy	CLS (eV)/FWHM (eV) of fitted S 2p components			
	B	S	M	HE
210 eV	0.00/ 0.77 ± 0.03	−0.64 ± 0.03/ 0.65 ± 0.02	−1.23 ± 0.04/ 0.55 ± 0.02	+1.75 ± 0.2/ 1.7 ± 0.3
350 eV	0.00/ 0.63 ± 0.01	−0.65 ± 0.05/ 0.53 ± 0.01	−1.25 ± 0.05/ 0.57 ± 0.02	+1.80 ± 0.1/ 2.2 ± 0.2
500 eV	0.00/ 0.78 ± 0.02	−0.67 ± 0.02/ 0.77 ± 0.02	−1.26 ± 0.02/ 0.60 ± 0.03	+1.80 ± 0.2/ 2.3 ± 0.3

listed explicitly in Table 2. Feature B ("Bulk"), distinguished by a 2$p_{3/2}$ peak centered at 162.8 eV binding energy (BE), is ascribed to the signal from bulk sulfur S$_2{}^{2-}$ dimers (see Fig. 3b). Feature S ("Surface") has a core level shift (CLS) of -0.65 ± 0.05 eV BE relative to B and represents surface S$_2{}^{2-}$ dimers (Fig. 3c). Finally, feature M ("Monomer") is at a CLS of -1.25 ± 0.05 eV BE relative to B and is related to the monomer defect (or monovacancy) species S^{2-} at the surface (Fig. 3d) which is of primary interest for this work.

Quantifying the temperature dependence of proportion of the M contribution in the S 2p spectrum enabled us to identify the sulfur vacancy formation enthalpy on the pyrite surface, as described below. An additional singlet peak, which we refer to as the 'high energy' (HE) peak was fit to each spectrum at 1.8 ± 0.2 eV above the main B peak, with a 70% Gaussian-30% Lorenztian distribution. Previous reports of the FeS$_2$(100) S 2p photoemission have either explicitly or implicitly dealt with a similar feature. For example, Nesbitt *et al.* fit a single peak in their work and attributed it
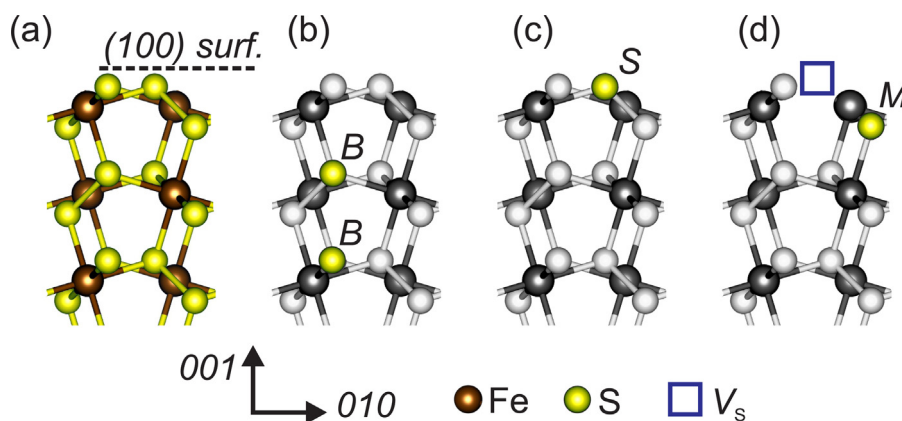

Fig. 3. (a) Atomic model of the FeS$_2$(100) surface as viewed side-on, with highlighted sulfur atoms corresponding to x-ray photoelectron spectroscopy features denoted as: (b) Bulk 'B' sulfur binding environment with 3 Fe-S bonds and 1 S-S bond, (c) surface 'S' environment with one fewer Fe-S bond, and (d), monomer 'M' with an adjacent sulfur vacancy and hence no S-S bond.
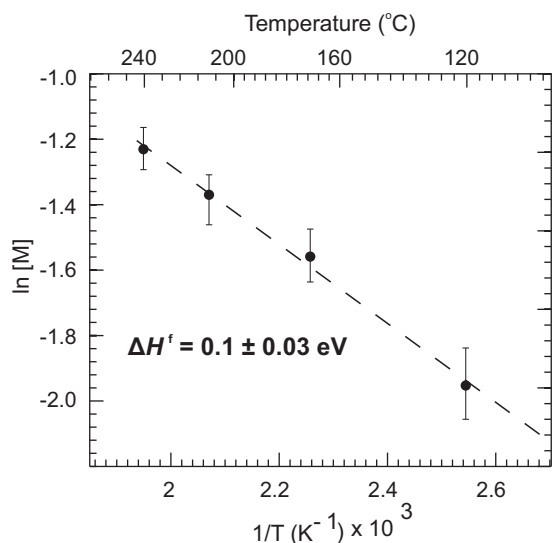
Fig. 4. Sulfur monomer vacancy concentration [M] as a percentage of total S 2p photoelectron spectrum signal vs. inverse temperature. The dashed line is the best linear fit to the data, and error bar generation is discussed in the text. ΔH^f is calculated from the slope of this line, assuming the Arrhenius relationship in Eq. (2).

to polysulfides (S_n^{2-}) [49], Mattila *et al.* stipulated the additional signal in this region to arise from the effect of the core hole [65], and Andersson *et al.* fitted their pyrite S 2p peaks with asymmetric tails towards higher binding energies to account for this contribution [48]. In our work, we did not observe the high-energy tail of the S 2p spectra to change significantly during the course of the annealing experiments from 120-350 °C. As the experiments were conducted under reducing UHV conditions we dismiss the possibility of surface S_n^{2-} contributing to the signal. We therefore postulate that the fitted *HE* component is generated by the core hole effect in pyrite, and we used systematic fitting parameters to remove the influence of this peak on the quantification of the other components *B*, *S* and *M*. The total intensity (area) of the *HE* peak was constrained to be 10% of the total S 2p signal and variation of this constraint by ± 5% had no quantitative effect on the relative proportions of the *B*, *S* and *M* features fitted on each spectrum. The surface sensitivity of XPS is related to the inelastic mean free path λ of the emitted photoelectrons. To minimize λ, the incident photon energy is chosen such that the kinetic energy of the excited photoelectron is of the order 40-50 eV [46]. For the S 2p peak at a BE of ~160 eV this corresponds to an x-ray excitation energy hν of 200-210 eV. Hence the spectra in Fig. 2c and 2d obtained using hν = 210 eV originate from the top 4.5 ± 1 Å (2-3 sulfur layers) while those in Fig. 2a and 2b at hν = 350 eV are attributable to the top 11 ± 1 Å (4-5 sulfur layers). For the other excitation energy used in this work, hν = 500 eV, the estimated λ is 14 ± 1 Å (5-6 sulfur layers). At the 500 eV photon energy, the surface sulfur species of interest to this work have relatively weak signal as compared to the bulk species *B*; therefore we do not include the 500 eV XPS results in further discussion. Features *S* and *M* are most prominent in Fig. 2c and 2d which were obtained using 210 eV excitation energy, indicating that these signals arise from the 1-2 atomic layers of pyrite closest to the (100) free surface of the crystal. As can be seen in the deconvoluted XPS spectra in Fig. 2, the proportion of *M* as a fraction of the total S 2p signal, denoted as [M], increases with increasing annealing temperature up to 330 °C. This trend is consistent with the formation of surface monomer defects as the sample surface is increasingly chemically reduced. In the intermediate temperature region between 120-240 °C, [M] increased consistently with temperature (Fig. 4).

To estimate the formation enthalpy of sulfur monomer vacancies, [M] in the most surface-sensitive measurement (hν = 210 eV) was quantified as a function of temperature. We assume the following simple defect reaction to form electronically neutral vacancies under UHV annealing:

$$FeS_2 \rightarrow Fe_{Fe}^x + S_{S_i}^x + V_{S_{ii}}^x + \frac{1}{2}S_2(g), \tag{1}$$
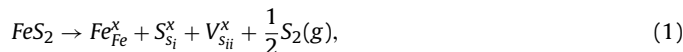
where the conventional Kröger-Vink notation[66] is used and the subscripts S_i and S_{ii} refer, in no particular order, to the two adjacent sulfur sites on any given anion dimer. Although the formal oxidation state of the newly formed sulfur monomer site (S_{ii} here) should be S^{1-}, it is understood this configuration relaxes to the more stable S^{2-} by electron transfer from an adjacent cation, leaving the vacant site electronically neutral [49,67]. We write the Gibbs free energy change of the defect formation reaction in Eq. (1) as $\Delta G^f = \Delta H^f - T \Delta S^f$, where ΔH^f and ΔS^f are the enthalpy and entropy of vacancy formation, respectively. The sulfur vacancy concentration at a given temperature T can then be written:

$$[V_s] = \exp\left\{\frac{-\left[\Delta H^f - T\Delta S^f\right]}{k_B T}\right\} \cdot P_{S_2}^{-1/2}, \tag{2}$$

where k_B is Boltzmann's constant, P_{S_2} is the equilibrium partial pressure of sulfur gas, and we assume the activities of the solid to be unity. Finally, we note that a given change in [M] can be used as an estimate for change in $[V_s]$, if we apply the reasonable assumption that the only defect species contributing to the increase in [M] is the monomer vacancy, V_s.

Fig. 4 shows the results for the increase in relative contribution attributed to *M*, as ln[M] vs. 1/T, in the annealing temperature range of 120-240 °C. We present only the data obtained with 210 eV XPS excitation energy which gives the most surface sensitive results. From the slope of the straight-line fit and Eq. (2) we infer the formation enthalpy ΔH^f to be 0.1 ± 0.03 eV. Our estimated error in ΔH^f is the difference between maximum and minimum slope fits obtained from systematic variations in software-generated quantification of S 2p peak fits (including sensitivity to the selection of the *HE* fitted component, giving rise to the error bars detailed in Fig. 4 and Fig. 5), and does not reflect experimental error associated with the sample, equipment or measurement. The optimal peak fit for each component was first chosen so as to minimize the total root mean squared error between fitted data and experimental data. Error bars were then generated by methodically varying the peak positions of the *M* and *S* components relative to the position of *B*, across the ranges listed in Table 1; we believe this gives a reasonable quantitative estimate of fitting error. However, in this quantification we neglect any clustering of defects at lower temperatures that would effectively suppress the value of [M], as discussed in more detail below. This is reasonable given the high resolution achieved in our STM images, which suggest that these surfaces are not likely to have many small clusters at the lower temperatures. As a result, the calculated ΔH^f may only slightly underestimate the true activation enthalpy for vacancy formation.

Upon annealing to higher temperatures (240 °C-330 °C) we observed a noticeable deviation from the Arrhenius behavior of [M] that is seen in Fig. 4. Fig. 5a shows that the percentage of *M* reached a maximum at around 240 °C and then dropped by ~ 3-4% of total S 2p signal, before leveling off to a roughly constant value for temperatures above 270 °C. Furthermore, the total signal arising from the *S* component increased in this temperature range up to 270 °C, by a roughly equivalent amount (~10%) to *M*, then leveled to a consistent value of around 43% of the total S 2p signal between 270-330 °C (Fig. 5b). Such non-Arrhenius behavior of [M] and [S] imply a more complicated phenomenon than the otherwise logical hypothesis that surface-localized sulfur dimers (*S*) are converted
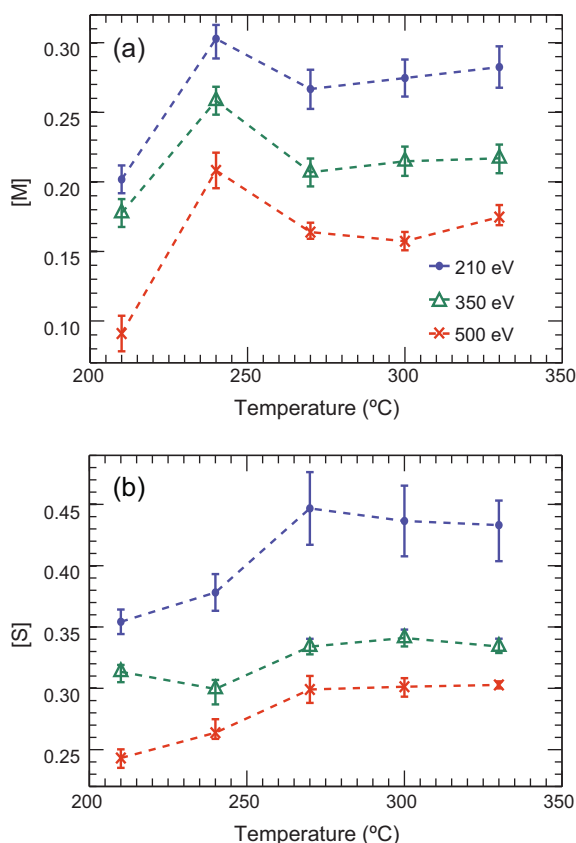
Fig. 5. The proportion of the M and S components of the S 2p photoelectron spectra on FeS$_2$ (100) at 200-330 °C, measured using three different excitation energies: 210, 350 and 500 eV. (a) The fraction of the total signal represented by M increased up to 270 °C then dropped and stayed approximately constant, (b) The fraction of total signal represented by S also increased up to 270 °C but then remained unchanged to 330 °C. The dashed lines connecting the data points are shown as a guide for the eye.

directly to monomers (M) by the thermally-assisted breaking of the sulfur-sulfur bonds; in such a case we would expect any increase in M signal to be matched by a corresponding drop in S. We will revisit the mechanisms that could explain such a non-monotonic change in sulfur monovacancies via later description of kMC simulations. However, the model underlying such computational simulations is informed by direct observation of the surface reconstruction of pyrite, which we next address.

Scanning tunneling microscopy (STM) images of single crystal pyrite (100) surfaces both at room temperature and after *in situ* annealing to 220 °C and to 300 °C for >150 min (Fig. 6) provided further details on the behavior of defects underlying the results in Fig. 5. For comparison, we include predictions from our temperature-dependent kMC simulations of point defect formation and clustering. These simulated results are discussed in more detail in the following section. The initial surface condition of the FeS$_2$ single crystals consisted of multiple atomically-flat, featureless (100) terraces (Fig. 6a, 6b, 6c). After annealing at 220 °C in UHV, we observed two notable changes in surface morphology: first, the straight ledges separating atomic terraces became wavy, with small incursions into the terrace (Fig. 6d). Second, there appeared multiple small, irregularly-shaped depressions on the surface of flat terraces that arose from the agglomeration of surface anion and cation vacancies (Fig. 6e, 6f), henceforth referred to as vacancy clusters or 'pits'. At 220 °C we observed a dispersion of cluster sizes (widths) from smaller than 1 nm to ∼10 nm (Fig. 6e). Following annealing at 300 °C, these grew to form a more homogeneous spread of clusters with lateral dimensions consistently

between 5-10 nm (Fig. 6g, 6h, 6i). As described in Section 2.1, we believe the source of the observed iron vacancies (V_{Fe}) to be supersaturated V_{Fe} remaining in the bulk after crystal synthesis under high sulfur chemical potential μ_S. During annealing in the low μ_S experimental conditions in UHV, iron vacancies migrate to the surface to equilibrate a stoichiometric bulk rid from V_{Fe}. This process effectively 'provides' cation vacancies to the surface, leading to a situation similar to the dissolution of metal cations into liquid electrolytes in contact with a passive film [68,69]. Similar surface vacancy clusters have been observed on metals containing supersaturated vacancies from quenching [19,70,71], nonstoichiometric oxides such as CeO$_2$ [72–74] and also natural pyrrhotite Fe$_{1-x}$S that have been subjected to heating under vacuum.

The pits exhibited a curved, non-faceted morphology that can be rationalized by comparison to the curved terrace steps observed by Rosso et al. on conchoidal fracture surfaces of FeS$_2$ [44]. Normal to the free surface of the crystal, the depth of the defect clusters also changed between 220-300 °C, as seen in the image height histograms of Fig. 7a. After *in situ* annealing treatment at 220 °C, there existed a bimodal distribution of pit depths, with the majority of pixels at the nominal surface level (normalized to 0 nm on the scale shown) and a subset located at a depth of approximately 0.25 nm.

After *in situ* annealing at 300 °C, the pit depth distribution broadened and the mean depth of the minor peak in the histogram is shifted to approximately 0.55 nm. The line traces in Fig. 7b and 7c provide more detail on the depth of pits: at 220 °C the surface pits were consistently 2.7 ± 0.1 Å deep whereas at 300 °C the majority of pits have a depth of 5.4 ± 0.1 Å. Given the lattice parameter of pyrite of 5.41 Å [75], these pit depths correspond to one half and one full lattice parameter, respectively.

3.2. Mechanism of vacancy formation and coalescence

The growth of defect clusters as evidenced by our STM results, along with the XPS results presented in Figs. 4 and 5, lead us to propose a mechanism involving three distinct phenomena occurring in tandem during the *in situ* reduction of the FeS$_2$(100) surface, as visualized in Fig. 1:

(i) formation of isolated S monovacancies (V_S) and surface-ward migration of Fe vacancies (V_{Fe}) from the bulk, giving rise to increasing signals of sulfur species M and S, respectively;

(ii) surface diffusion of V_S and V_{Fe}, followed by the stochastic clustering of small numbers of vacancies;

(iii) growth of vacancy clusters, which are more stable geometric features for the reduced surface compared to dispersed point defects, due to a reduced formation energy for sulfur vacancies at step edges.

The proposed mechanism was cast into our kinetic Monte Carlo model as described in Section 2.3. The last row of images in Fig. 6 shows the successive formation and growth of surface pits after simulated annealing for 4 h. The model reproduces the flat, nearly featureless surface at ambient temperatures (Fig. 6c), while a series of pits with average lateral dimension of 1×1 nm^2 becomes visible at 220 °C (Fig. 6f) and larger pits on the order of 2×2 nm^2 at 300 °C (Fig. 6i). Similar to the case of STM images, individual vacancies are not displayed on the simulated surfaces; only the agglomeration of several vacancies is visible. Each simulation in reality contains a distribution of V_S defects that were statistically averaged over eight simulation runs to provide a simulated estimate of the V_S concentration at each temperature of interest. This was compared to the experimentally measured value [M] obtained by XPS. We note that although the transition to pitting (Fig. 6) and the total concentration of M sites (Fig. 8) are predicted reasonably well by this kMC simulation, the pit width is not correctly predicted. We
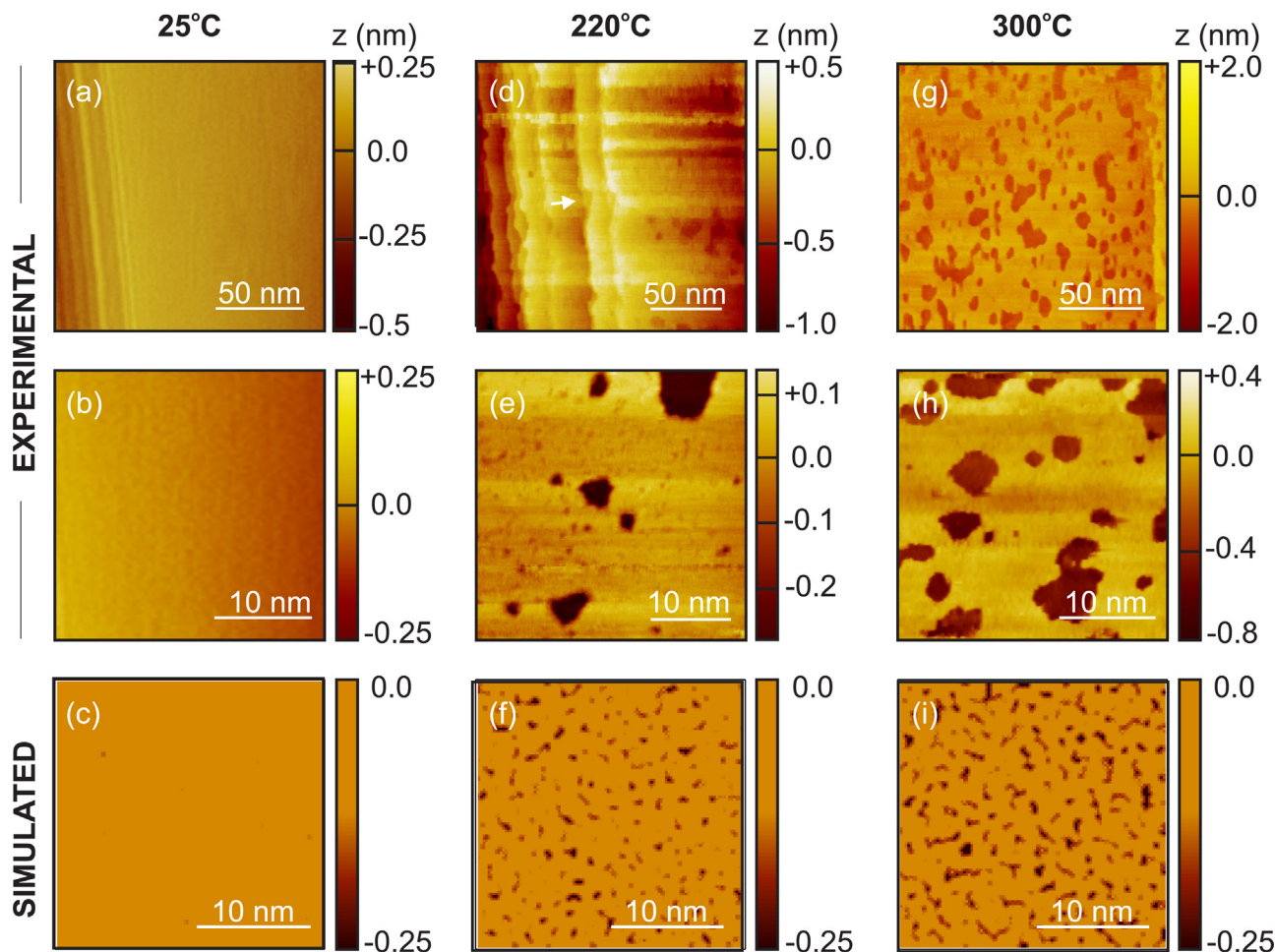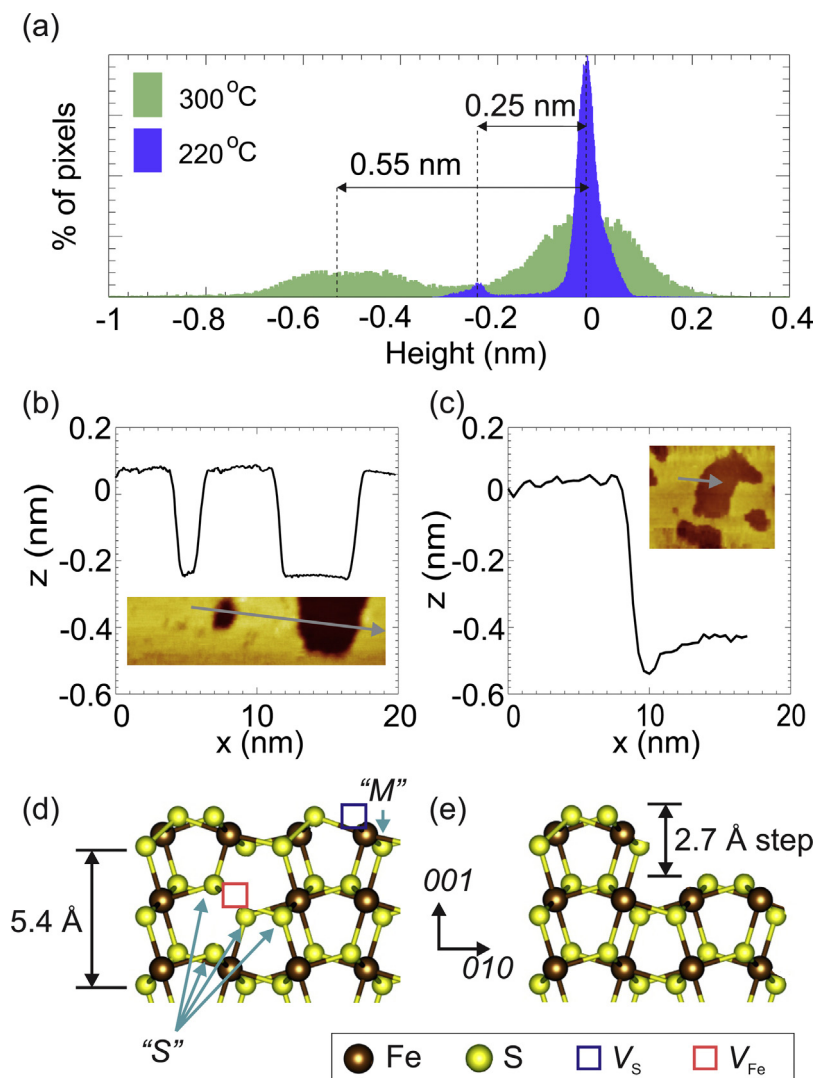
Fig. 6. Scanning tunneling microscopy (STM) images of single crystal FeS$_2$(100) surfaces [(a), (b)] prior to any *in situ* annealing in ultra high vacuum, [(d), (e)] after three hours of *in situ* annealing at 220 °C, and [(g), (h)] after three hours at 300 °C. The surface morphology of atomically-flat terraces at room temperature changes under annealing due to the formation of vacancy clusters. In addition, originally straight terrace edges–visible in the bottom left corner of (a)–develop into wavy lines, e.g. as indicated by the white arrow in (d). All STM data were collected at room temperature using tunneling conditions in the range ±(1-2) V and 200-1000 nA. The bottom row of images [(c), (f), (i)] display the results of kinetic Monte Carlo (kMC) simulations performed at the same temperatures of (c) 25 °C, (f) 220 °C and (i) 300 °C for comparison with the experimental images. The activation barrier values used in these kMC simulations are taken to be the mean of the range given in Table 1: $V_{S,form} = 1.62$ eV, $V_{S,anni} = 1.62$ eV, $V_{Fe,form} = 1.54$ eV, $V_{Fe,anni} = 1.64$ eV, $V_{diff} = 1.45$ eV. See Figure S4. in the Supplementary Information for alternative parameters used and the resulting surface pit sizes.

think this difference is because of the large energy barrier predicted by DFT for defect migration on the surface. However, the growth rate of the relative size of kMC-simulated pits with temperature is comparable to that of those in the STM images. Table S1 in the Supplementary Information file shows black and white images from Fig. 6, together with average pit sizes for each. In Figure S3 it can be seen that the rate of pit growth (relative size) with temperature is very similar with both sets of data. This should be attributed to the use of the vacancy formation enthalpy value found from XPS experiments in the kMC simulations. Therefore, while the absolute sizes found in experiments and in simulations differ from each other, the effective dependence on temperature is the same, suggesting that the dominant mechanism is captured consistently.

One key feature of our experiments was that the concentration of the sulfur monovacancy [M] changed non-monotonically with temperature, peaking at ~250 °C annealing temperature. The calculated monovacancy concentrations from the kMC model are shown in Fig. 8. The most surface sensitive XPS measurement of the monovacancy concentration from Fig. 5 is also plotted here for comparison. The resulting range, depicted as the blue shaded zone in Fig. 8, represents the broadest envelope of variations in the

monovacancy concentrations as the individual barriers were varied over the range shown in Table 1. Between 200-250 °C the model predicts an increase in [M], consistent with the formation of individual surface V_S at a rate that exceeds the rate of their condensation into pits. At 250 °C and above, the stochastically created monovacancies are sufficiently numerous and densely spaced for agglomeration processes to occur. At these temperatures, further individual vacancy formation occurs more favorably at the step edges of the newly created pits. In addition, the rapid diffusion of point defects at these elevated temperatures allows pits to grow further by vacancy coalescence. Together, these two effects can account for the drop in [M] observed in the experimental result, as shown by the upper bound of the simulated results. Depending on the exact values of activation energies assumed, the behavior may also increase monotonically as shown by the lower bound of the simulated results. Finally, with increasing temperatures up to 330 °C, [M] becomes relatively stable, due ostensibly to a dynamic equilibrium between thermally activated individual vacancy formation and pit growth by a combination of vacancy formation at step edges of pits and rapid diffusion. The result is a non-Arrhenius dependence of vacancy concentration on temperature, captured both in experiments and kMC simulations.

Fig. 7. (a) Height (z-axis) histograms of scanning tunneling microscopy images obtained after annealing at 220 °C (and at 300 °C bimodal distributions of pit depths are observed at both annealing temperatures; however the average pit depth is ∼0.25 nm in the former case and ∼0.55 nm in the latter. (b) Line trace (gray arrow) of height acquired across the pit-like features taken from Fig. 6(e), inset, showing pits of depth $a/2 = 0.25$ nm, where a is the FeS$_2$ lattice parameter. (c) Line trace of height acquired across feature in Fig. 6(h), inset; the depth at this higher annealing temperature is $a = 0.54$ nm. Atomic structure schematics of the (100) surface, as a side view, illustrate (e) the formation of new M and S feature environments surrounding iron and sulfur vacancies (V_{Fe} and V_S, respectively), and (e) the formation of a surface step of $a/2$ height by the clustering of near-surface iron and sulfur vacancies.
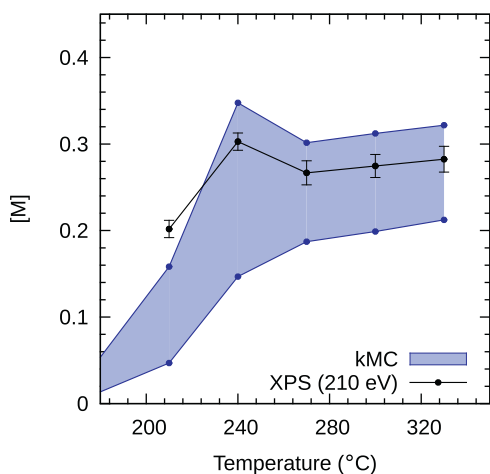
Below, we discuss in more detail the three phenomena that account for this pit initiation mechanism:

(i) <u>Formation of sulfur and iron vacancies at and near the surface:</u> Elemental sulfur is highly volatile in comparison to iron, with a melting temperature of 115 °C at 1 atm pressure. We therefore assume sulfur sublimes from pyrite and is dynamically removed from the sample surface under vacuum until the pyrite equilibrates with the ambient sulfur chemical potential, dictated by the chamber pressure of ∼10^{-9}-10^{-10} mbar. We also noted the importance of iron vacancies in our model. The corresponding appearance of V_{Fe} near the surface is indicated by the growth of the S feature of the XPS S $2p$ spectra while the surface is increasingly reduced. Fig. 7d illustrates how six new S binding environments would accompany the introduction of a single V_{Fe} in the second atomic layer from the (100) surface (NB: only 4 S sites are shown in the plane of the graphic). Since Fe loss through evaporation into vacuum is unlikely at the relatively low annealing temperatures compared to

the melting point T_m of iron (300 °C < 0.2 T_m), the increase of V_{Fe} requires an alternative explanation. It is known that the formation enthalpy of the V_{Fe} in pyrite increases by up to 1.42 eV as the environment changes from a sulfur-rich one to one deficient in sulfur [52]. This large change implies that the sizable number of V_{Fe} defects originally present in the pyrite crystal during synthesis in sulfur-rich conditions are not stable in the sulfur-deficient conditions encountered during the annealing process. In order to equilibrate the bulk under these experimental conditions, the oversaturated V_{Fe} point defects migrate from bulk towards the free surface at high temperatures to annihilate. In providing iron vacancies to the surface, coincidentally in this work, the situation is analogous to the dissolution of metal cations from the passive film in liquid electrolytes [68].

(ii) <u>Diffusion of sulfur and iron vacancies on the surface:</u> The generation of incursions into pre-existing atomic terrace edges (Fig. 1d) and the nucleation of small vacancy clusters on top of terraces (e.g., as seen in Fig. 1e), requires the diffusion of both

be 0.1 ± 0.03 eV from the exponential temperature dependence of the sulfur monomer vacancy (V_S) binding environment detected in the S $2p$ photoelectron spectra measured by synchrotron XPS. However, at higher temperatures above 200 °C, the sulfur vacancy concentration decreased and deviated from the Arrhenius behavior, concurrent with the initiation of nanometer-scale surface pits. The depths of these pits were exactly one-half or one FeS_2 lattice parameter, as imaged by STM. To explain this behavior, we propose a mechanism involving the simultaneous formation and migration of vacancies at the surface, with facilitated vacancy formation and agglomeration at step edge sites surrounding pits. A simple kinetic Monte Carlo simulation with thermally activated reactions was used to validate the proposed mechanism. The high sensitivity of the model to the energy barrier parameters used highlights the need for understanding the atomic details responsible for these processes before purely DFT-derived barriers can be used in time-evolution models such as kMC.

We note two important implications of these findings. First, the observed, concerted agglomeration of point defects from both cation and anion sublattices to initiate nanoscale pits has broad consequences for ionic solids in reducing environments. The dynamics of surface point defects observed under controlled reducing environments offer an atomistic level description of the incipient stages of pit formation in passive films, as postulated in models of surface degradation such as the Point Defect Model. Second, the relatively low defect formation energy that we measure for sulfur vacancies confirms the high chemical reducibility of the FeS_2 surface, often linked to poor electronic [14] and electrochemical properties [15] in synthetically grown pyrite.

Acknowledgments

Appendix A. Supplementary data

Supplementary data associated with this article can be found, in the online version, at http://dx.doi.org/10.1016/j.electacta.2014.02.048.

References

[1] H. Vedage, T.A. Ramanarayanan, J.D. Mumford, S.N. Smith, Corrosion 49 (1993) 114–121.
[2] J. Bebie, M.A. Schoonen, Geochemical Transactions 1 (2000) 47.

Fig. 8. Simulated values of the sulfur monomer vacancy concentration [M] on the pyrite surface as a function of annealing temperature, obtained by kinetic Monte Carlo simulations (kMC) and indicated by the blue zone. The width of predicted [M] indicated by this blue band is given by variation in kMC energy barrier values over the range described in Table 1. Values of [M] experimentally determined from our XPS measurements (Fig. 5a) are shown for comparison.

V_{Fe} and V_S across the surface. When two or more vacancies encounter each other stochastically, a small cluster is formed which is more stable relative to the dispersed individual vacancies. STM imaging by Rosso et al. has recorded surface diffusion of iron vacancies on natural single crystals of FeS_2 at room temperature over time scales of minutes, so diffusive processes are expected to occur with low energy barriers [43]. In the kMC model in this work, a higher barrier was taken for diffusion of vacant surface sites away from the pits compared to diffusion of vacancies towards the pits, simulating the trapping of vacant sites by the initiated pits.

(iii) Growth of pits: Once a stable pit nucleates, the reduced coordination of sulfur atoms at the newly-created step edges of pits (Fig. 7e) facilitates vacancy formation by reducing the formation energy for vacancies, and accelerates the growth of pits. Indeed, our DFT calculations showed that ΔH^f for individual V_S at a step edge of a pit could be up to ~40% lower than that on an atomically-flat surface. This type of dependence of defect formation on the local atomic configuration has also been observed in sulfide inclusions in pitting corrosion [76].

The formation and expansion of surface vacancy clusters in this manner provides an explanation for the surprisingly low ΔH^f for sulfur vacancies of around 0.1 eV that we measured using XPS below 240 °C (Fig. 4), as compared to recent theoretical predictions in the range of 0.4-1.44 eV [35,36,52]. Upon raising the temperature to greater than 240 °C, the effect of growing the vacancy clusters is to maintain the XPS signal intensity from M at a roughly constant value. This is because the removal of a sulfur atom from the step edge of a vacancy cluster, while growing the cluster, does not result in the creation of an adjacent monomer M site on the surface structure; therefore the M signal intensity does not increase in the S $2p$ spectrum.

4. Conclusions

We have investigated the evolution of surface chemistry and morphology on synthetic pyrite single crystals as a function of annealing temperature in reducing conditions, in order to visualize and quantify the mechanisms leading to pit initiation on the surface. Formation enthalpy for sulfur vacancies was found to

[3] D.K. Nordstrom, C.N. Alpers, Proceedings of the National Academy of Sciences of the United States of America 96 (1999) 3455–3462.
[4] K.R. Popper, Nature 344 (1990), 387-387.
[5] M.G. Gong, A. Kirkeminde, N. Kumar, H. Zhao, S.Q. Ren, Chemical Communications 49 (2013) 9260–9262.
[6] Y. Shao-Horn, Q.C. Horn, Electrochimica Acta 46 (2001) 2613–2621.
[7] E. Peled, D. Golodnitsky, E. Strauss, J. Lang, Y. Lavi, Electrochimica Acta 43 (1998) 1593–1599.
[8] S.G. Choi, J. Hu, L.S. Abdallah, M. Limpinsel, Y.N. Zhang, S. Zollner, R.Q. Wu, M. Law, Physical Review B 86 (2012).
[9] A. Ennaoui, S. Fiechter, C. Pettenkofer, N. Alonsovante, K. Buker, M. Bronold, C. Hopfner, H. Tributsch, Solar Energy Materials and Solar Cells 29 (1993) 289–370.
[10] J. Puthussery, S. Seefeld, N. Berry, M. Gibbs, M. Law, Journal of the American Chemical Society 133 (2011) 716–719.
[11] N. Berry, M. Cheng, C.L. Perkins, M. Limpinsel, J.C. Hemminger, M. Law, Advanced Energy Materials (2012).
[12] Y. Bi, Y.B. Yuan, C.L. Exstrom, S.A. Darveau, J.S. Huang, Nano Letters 11 (2011) 4953–4957.
[13] C. Wadia, Y. Wu, S. Gul, S.K. Volkman, J.H. Guo, A.P. Alivisatos, Chemistry of Materials 21 (2009) 2568–2570.
[14] P. Lazic, R., Armiento, F.W., Herbert, R., Chakraborty, R., Sun, M., Chan, K., Hartman, T., Buonassisi, B., Yildiz, G. Ceder, Journal of Physics: Condensed Matter, 25 (2013).
[15] F.W. Herbert, A., Krishnamoorthy, K.J. Van Vliet, B., Yildiz, Surface Science, 618 (2013) 53-61.
[16] D.D. Macdonald, Electrochimica Acta 56 (2011) 1761–1772.
[17] D.D. Macdonald, Journal of The Electrochemical Society 139 (1992) 3434–3449.
[18] C. Zhang, K.C. Chan, Y. Wu, L. Liu, Acta Materialia 60 (2012) 4152–4159.
[19] J.R. Jasperse, P.E., Doherty, Philosophical Magazine, 9 (1964) 635-&.
[20] G. Rosenfeld, K. Morgenstern, M. Esser, G. Comsa, Applied Physics A 69 (1999) 489–496.
[21] K. Morgenstern, Physica Status Solidi (b) 242 (2005) 773–796.
[22] Z. Zhang, J.S. Pan, J. Zhang, E.S. Tok, Physical Chemistry Chemical Physics 12 (2010) 7171–7183.
[23] B.K. Tariyal, B. Ramaswami, Applied Physics Letters 16 (1970) 227–228.
[24] B.K. Tariyal, B. Ramaswami, Journal of Applied Physics 42 (1971) 948–952.
[25] T. Massoud, V. Maurice, F. Wiame, L.H. Klein, A. Seyeux, P. Marcus, Journal of The Electrochemical Society 159 (2012) C351–C356.
[26] P. Marcus, V. Maurice, H.H. Strehblow, Corrosion Science 50 (2008) 2698–2704.
[27] A.H. Heuer, H. Kahn, F. Ernst, G.M. Michal, D.B. Hovis, R.J. Rayne, F.J. Martin, P.M. Natishan, Acta Materialia 60 (2012) 716–725.
[28] P. Meakin, K.M. Rosso, The Journal of Chemical Physics 129 (2008) 204106–204119.
[29] H. Zhou, J. Fu, R.M. Silver, The Journal of Physical Chemistry C 111 (2007) 3566–3574.
[30] R.S. Lillard, G.F. Wang, M.I. Baskes, Journal of the Electrochemical Society 153 (2006) B358–B364.
[31] L.A. Li, G.W. Zhou, Surface Science 605 (2011) 54–61.
[32] L. Klinger, I. Gotman, E. Rabkin, Scripta Materialia 67 (2012) 352–355.
[33] M. Birkholz, S. Fiechter, A. Hartmann, H. Tributsch, Physical Review B 43 (1991) 11926.
[34] R.S. Sun, M.K.Y. Chan, S.Y. Kang, G. Ceder, Physical Review B 84 (2011).
[35] L.P. Yu, S. Lany, R. Kykyneshi, V. Jieratum, R. Ravichandran, B. Pelatt, E. Altschul, H.A.S. Platt, J.F. Wager, D.A. Keszler, A. Zunger, Advanced Energy Materials 1 (2011) 748–753.
[36] J. Hu, Y.N. Zhang, M. Law, R.Q. Wu, Physical Review B 85 (2012).
[37] H.A. Macpherson, C.R. Stoldt, ACS Nano 6 (2012) 8940–8949.
[38] Y. Bai, J. Yeom, M. Yang, S.-H. Cha, K. Sun, N.A. Kotov, The Journal of Physical Chemistry C (2013).
[39] C. Steinhagen, T.B., Harvey, C.J., Stolle, J., Harris, B.A. Korgel, The Journal of Physical Chemistry Letters, (2012) 2352-2356.
[40] M. Caban-Acevedo, M.S. Faber, Y.Z. Tan, R.J. Hamers, S. Jin, Nano Letters 12 (2012) 1977–1982.
[41] M. Cabán-Acevedo, D., Liang, K.S., Chew, J.P., DeGrave, N.S., Kaiser, S., Jin, ACS Nano, (2013).
[42] S. Chaturvedi, R. Katz, J. Guevremont, M.A.A. Schoonen, D.R. Strongin, American Mineralogist 81 (1996) 261–264.
[43] K.M. Rosso, U. Becker, M.F. Hochella, American Mineralogist 85 (2000) 1428–1436.
[44] K.M. Rosso, U. Becker, M.F. Hochella, American Mineralogist 84 (1999) 1535–1548.
[45] F.R. Fan, A.J. Bard, Journal of Physical Chemistry 95 (1991) 1969–1976.
[46] J.A. Leiro, S.S. Mattila, K. Laajalehto, Surface Science 547 (2003) 157–161.
[47] S. Mattila, J.A. Leiro, M. Heinonen, Surface Science 566 (2004) 1097–1101.
[48] K. Andersson, M. Nyberg, H. Ogasawara, D. Nordlund, T. Kendelewicz, C.S. Doyle, G.E. Brown, L.G.M. Pettersson, A. Nilsson, Physical Review B 70 (2004).
[49] H.W. Nesbitt, G.M. Bancroft, A.R. Pratt, M.J. Scaini, American Mineralogist 83 (1998) 1067–1076.
[50] A.H. Heuer, T. Nakagawa, M.Z. Azar, D.B. Hovis, J.L. Smialek, B. Gleeson, N.D.M. Hine, H. Guhl, H.S. Lee, P. Tangney, W.M.C. Foulkes, M.W. Finnis, Acta Materialia 61 (2013) 6670–6683.
[51] S.J. Zinkle, G.S. Was, Acta Materialia 61 (2013) 735–758.
[52] F.W.H. A. Krishnamoorthy, S., Yip, K.J. Van Vliet, B. Yildiz, Journal of Physics: Condensed Matter, 25 (2012) 045004.
[53] A.G. Schaufuss, H.W., Nesbitt, I., Kartio, K., Laajalehto, G.M., Bancroft, R., Szargan, Surface Science, 411 (1998) 321-328.
[54] W. Kohn, L.J., Sham, Physical Review, 140 (1965).
[55] P.E. Blöchl, Physical Review B 50 (1994) 17953.
[56] G. Kresse, J. Furthmüller, Computational Materials Science 6 (1996) 15–50.
[57] G. Kresse, J. Furthmüller, Physical Review B 54 (1996) 11169.
[58] J.P. Perdew, K. Burke, M. Ernzerhof, Physical Review Letters 77 (1996) 3865–3868.
[59] G. Henkelman, B.P. Uberuaga, H. Jónsson, The Journal of Chemical Physics 113 (2000) 9901–9904.
[60] H.J. Monkhorst, J.D. Pack, Physical Review B 13 (1976) 5188–5192.
[61] K. Momma, F. Izumi, Journal of Applied Crystallography 41 (2008) 653–658.
[62] M.H. Kalos, P.A. Whitlock, Monte Carlo methods, in: J. Wiley & Sons, New York, 1986.
[63] G. Russo, L.M. Sander, P. Smereka, Physical Review B 69 (2004).
[64] I. Uhlig, R. Szargan, H.W. Nesbitt, K. Laajalehto, Applied Surface Science 179 (2001) 222–229.
[65] S. Mattila, J.A. Leiro, K. Laajalehto, Applied Surface Science 212 (2003) 97–100.
[66] F.A. Kroger, The Chemistry of Imperfect Crystals, North Holland, Amsterdam, The Netherlands, 1964.
[67] Y.N. Zhang, J. Hu, M. Law, R.Q. Wu, Physical Review B 85 (2012).
[68] K.R. Hebert, S.P. Albu, I. Paramasivam, P. Schmuki, Nature Materials 11 (2012) 162–166.
[69] A. Seyeux, V. Maurice, P. Marcus, Journal of the Electrochemical Society 160 (2013) C189–C196.
[70] K. Yoshimi, S. Hanada, T. Haraguchi, H. Kato, T. Itoi, A. Inoue, Materials Transactions 43 (2002) 2897–2902.
[71] A. Uedono, Y. Yamashita, T. Tsutsui, Y. Dordi, S. Li, N. Oshima, R. Suzuki, Journal of Applied Physics 111 (2012).
[72] Y. Namai, K. Fukui, Y. Iwasawa, Journal of Physical Chemistry B 107 (2003) 11666–11673.
[73] H. Norenberg, G.A.D. Briggs, Surface Science 424 (1999) L352–L355.
[74] S. Torbrugge, M. Reichling, A. Ishiyama, S. Morita, O. Custance, Physical Review Letters 99 (2007).
[75] G.L. Zhao, J. Callaway, M. Hayashibara, Physical Review B 48 (1993) 15781–15786.
[76] S.J. Zheng, Y.J. Wang, B. Zhang, Y.L. Zhu, C. Liu, P. Hu, X.L. Ma, Acta Materialia 58 (2010) 5070–5085.